Supplementary Information

Two-step Sequential Reactions of Supercritical CO_2 and Photocatalysis for PET Degradation and Hydrogen Production

Yanbing Liu, Jinwen Shi*, Zitong Zhuang, Xing Kang, Wenbo Xiao, Binjiang Zhai, Mengyuan Zhu, Hui Jin, Liejin Guo

International Research Center for Renewable Energy (IRCRE), State Key Laboratory of Multiphase Flow in Power Engineering (MFPE), Xi'an Jiaotong University (XJTU), 28 West Xianning Road, Xi'an, Shaanxi 710049, China

**Corresponding authors: jinwen_shi@mail.xjtu.edu.cn*

Materials and reagents

Fig. S1 gives the molecular formula of PET raw material ($(C_{10}H_8O_4)_n$, 100 mesh, purchased from Hengfa Plastic Technology Co Ltd, Guangdong, China), and Table S1 gives the elemental analysis and proximate analysis of PET raw material. Commercial Degussa P25-type titania nanoparticles (P25), dimethyl sulfoxide (DMSO), and methanol were purchased from Sinopharm Chemical Reagent Co., Ltd. and used without further purification. Chloroplatinic acid hexahydrate ($H_2PtCl_6 \cdot 6H_2O$) was purchased from Sigma-Aldrich Co., Ltd. and prepared as an aqueous solution with a Pt concentration of 0.765 mg mL^{-1}. Deionized water with a resistivity of 18.25 MΩ·cm was used in all experiments.

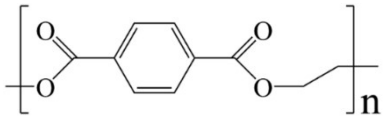

Fig. S1 Molecular formula of PET raw material.

Table S1 Elemental contents and chemical composition of PET raw material.

Sample	Elemental analysis (wt%)					Proximate analysis (wt%)			
	C_{ad}	H_{ad}	N_{ad}	S_{ad}	O_{ad}[a]	M_{ad}	A_{ad}	V_{ad}	FC_{ad}
PET	62.95	4.26	0.65	0.63	31.51	0.30	0.00	93.89	5.81

* [a]: By difference, $_{ad}$: air drying base.

Characterization details

The collected gas was determined using the gas chromatograph (GC, Agilent 7890, USA). The elemental contents of the PET raw material were determined using Elemental analyzer (EA, Elementar, vario MACRO cube, Italy) with He as carrier gas and O_2 as reaction gas. Powder X–ray diffraction (XRD) patterns were obtained with a diffractometer (PANalytical, X'pert MPD Pro, Netherlands) at 40 kV and 40 mA using Ni-filtered Cu Kα irradiation (λ = 1.5406 Å) and the scan range of 2θ = 10°–70° in steps of 5 °/min. Solid-state ^{1}H nuclear magnetic resonance (^{1}H NMR) spectra were taken on an NMR spectrometer (Bruker, Avance Neo 400 MHz, Germany). Fourier transform infrared (FTIR) spectra were recorded using an FTIR spectrophotometer (Bruker, Vertex 70, Germany) with the KBr pellet method. Brunauer–Emmett–Teller (BET) specific surface area measurements were performed using the Specific Surface Area and Porosity Analyzer (Micromeritics, ASAP 2460, USA) for N_2 adsorption, and all samples were degassed under a vacuum at 150°C for 12 h before N_2 adsorption. Scanning electron microscopy (SEM) was performed using a field-emission scanning electron microscope (JEOL, JSM-7800F, Japan). Thermogravimetric (TG) curves were recorded by a thermal analyzer (Mettler Toledo, TGA/DSC3+, Switzerland) in the range from 50°C to 800°C. Liquid products obtained from PET hydrolysis were determined by the gas chromatograph (GC 2002, Shanghai Kechuang, China). Solid products obtained from PET hydrolysis and liquid products after photocatalysis were analyzed by high-performance liquid chromatography (HPLC, Thermo Fisher Scientific, Germany) fitted with a full-scan dd MS^2 detector. The mobile phase A was deionized water and the mobile phase B was methanol.

Photocatalytic reaction measurement

Photocatalytic reaction was carried out in a Pyrex glass reactor (105 mL) using a 300 W Xe lamp as the light source. 50 mL of an aqueous solution that contained the pretreatment products was poured into the Pyrex glass reactor, followed by 30 mL of deionized water, and then 100 mg of P25 and 1 wt% (based on the weight of the catalyst) of an aqueous solution of H_2PtCl_6 were added sequentially. Before the reaction, the photocatalytic reactor was purged with Ar for 15 min to eliminate air. During the reaction, the solution temperature was maintained at 35^{o}C by circulating water and was stirred continuously. The evolved gas was detected using a North Point NP-GC-901A gas chromatograph (Ar as carrier gas, thermal conductivity detector (TCD), TDX-01 column), and each sample was measured twice to obtain an average value.

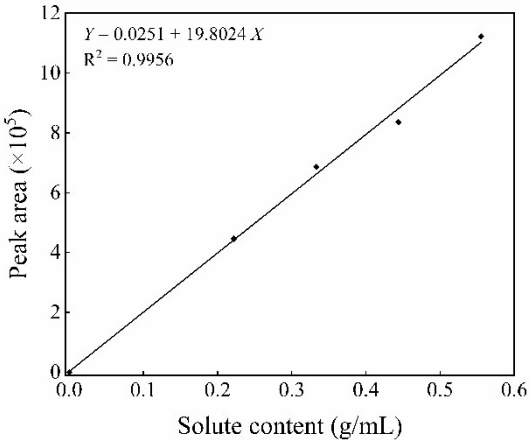

Fig. S2 Standard curve of ethylene glycol (EG).

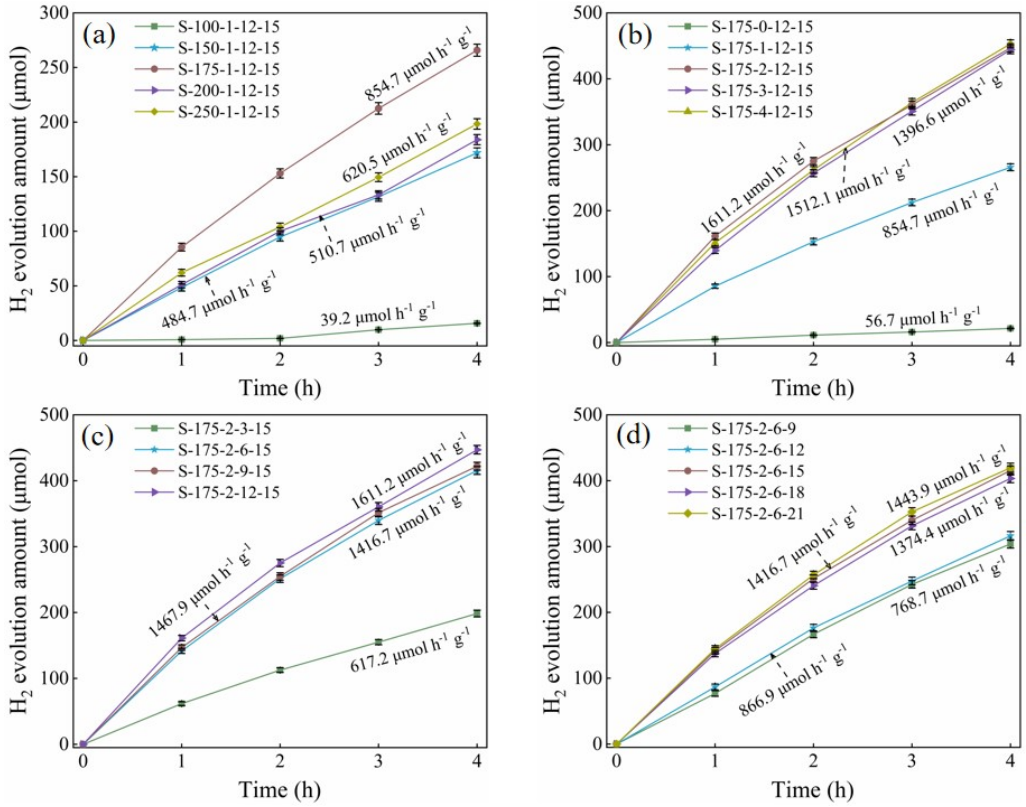

Fig. S3 H_2 evolution curves of S-*T*-*m*-*t*-*p* samples in photocatalytic reaction at different (a) pretreatment temperature, (b) mass ratio of H_2O/PET, (c) pretreatment time, and (d) pretreatment pressure.

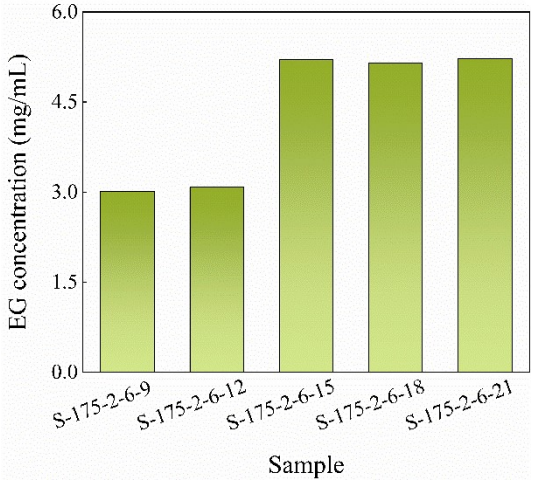

Fig. S4 Concentrations of EG in the liquid products (50 mL of solution).

Sun et al.[1] investigated the density variation of $ScCO_2$ with pressure over the temperature range of 300–900 K, revealing a positive correlation between density and pressure, and the results are listed in Table S2. Although data on the diffusivity of $ScCO_2$ at the same temperature were relatively limited, extensive literature indicated that the diffusivity of $ScCO_2$ exhibited a negative correlation with fluid density[2-5].

Table S2 Properties of $ScCO_2$ at different pressures (at 450 K)[1].

Pressure (MPa)	Density (kg m^{-3})
8	~109
10	~140
12	~172
14	~205
16	~238
18	~272
20	~305

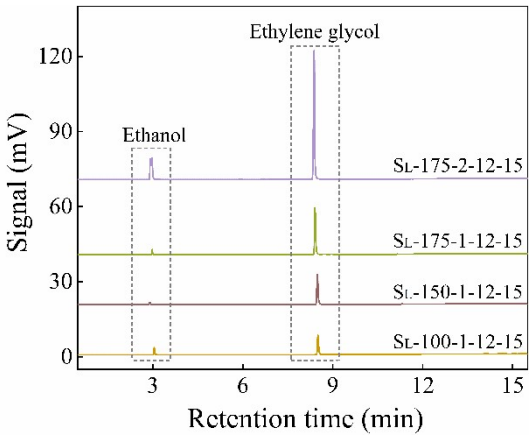

Fig. S5 GC signals of S_L-*T*-*m*-*t*-*p* samples. The signals were shifted upward in order by 0, 20, 40, and 70 mV, respectively.

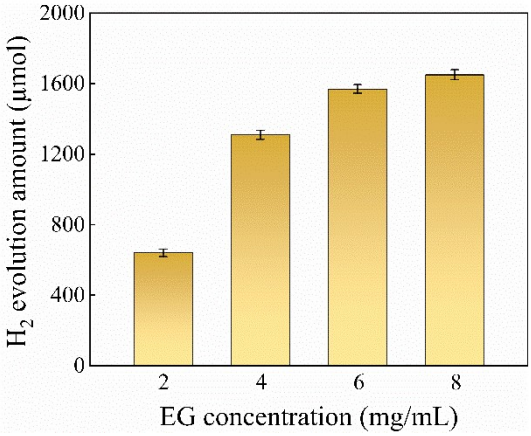

Fig. S6 H_2 evolution amounts of commercial EG in photocatalytic reaction within 4 h.

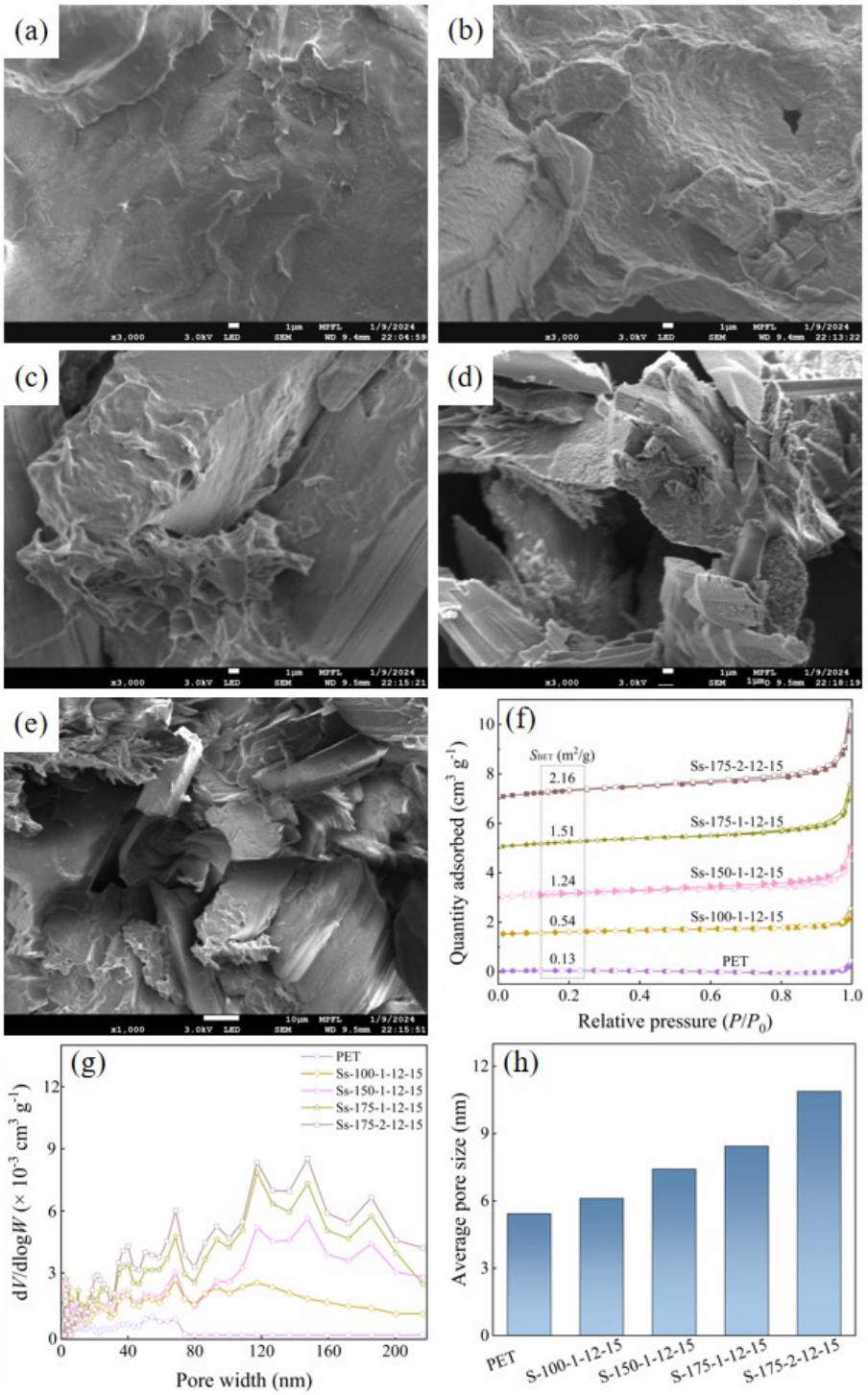

Fig. S7 SEM images of (a) PET, (b) Ss-100-1-12-15, (c) Ss-150-1-12-15, (d) Ss-175-1-12-15, and (e) Ss-175-2-12-15. Scale bar in (a-e): 1 μm. (f) N_2 adsorption-desorption isotherms and corresponding calculated BET surface areas, (g) pore size distribution curves, and (h) average pore sizes of PET and S_S-*T*-*m*-*t*-*p* samples. The isotherms of samples in (f) were shifted upward in order by 0, 1.5, 3, 5 and 7 cm^3 g^{-1}, respectively.

In Fig. S8a, commercial terephthalic acid (TPA) exhibited characteristic diffraction peaks at 2θ = 17.4°, 25.2° and 27.9°, corresponding to the (110), (011) and (200) crystal planes, respectively. The FTIR spectra in Fig. S8b showed that commercial TPA exhibited a strong absorption peak at 1282 cm^{-1} corresponding to C–O stretching vibration, a distinct carbonyl absorption band at 1680 cm^{-1}, and a broad peak characteristic of carboxylic acid hydroxyl groups in the 2200 cm^{-1}–3200 cm^{-1}. Additionally, the ^{1}H NMR spectra in Fig. S8c revealed that the H signal of benzene ring was located at approximately 10.3 ppm, while the proton signal of carboxyl group appeared at around 16.8 ppm. The TG curves in Fig. S8d indicated that commercial TPA began rapid weight loss starting at 230°C and completed decomposition at approximately 350°C, with the weight loss rate significantly accelerating during the decomposition phase. The above analysis demonstrated that the solid products obtained from the hydrolysis of PET in $ScCO_2$ exhibited functional group characteristics highly consistent with commercial TPA.

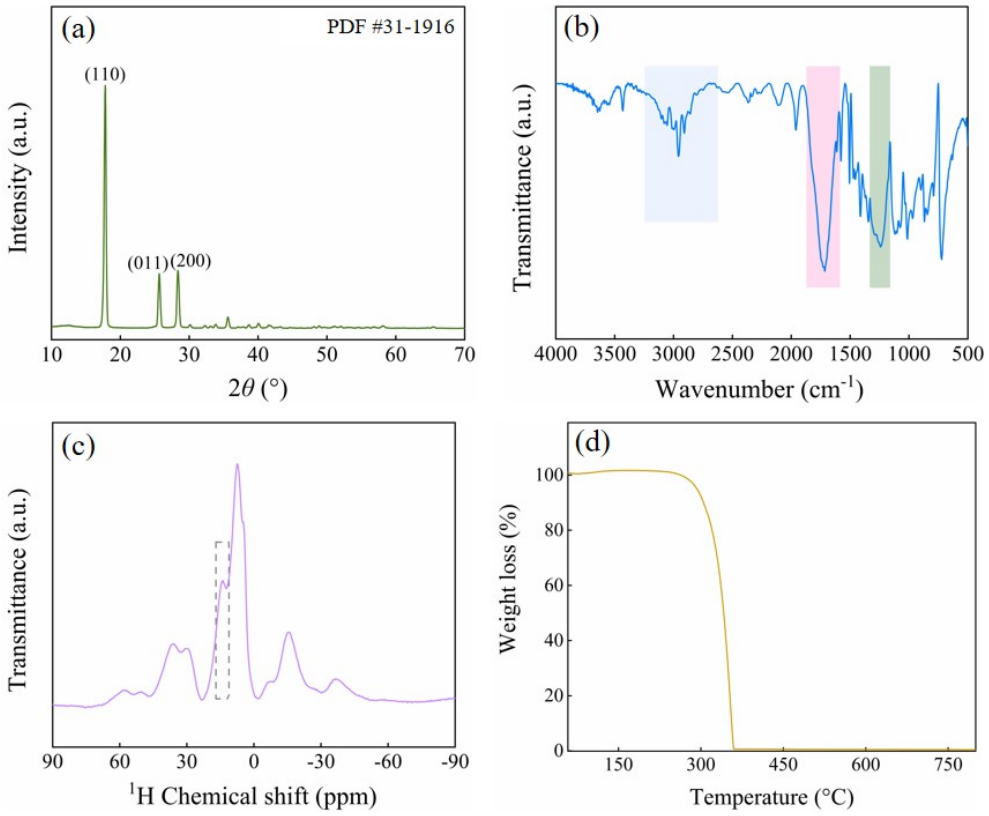

Fig. S8 (a) XRD patterns, (b) FTIR spectra, (c) solid state ^{1}H NMR spectra, and (d) TG curves of commercial TPA.

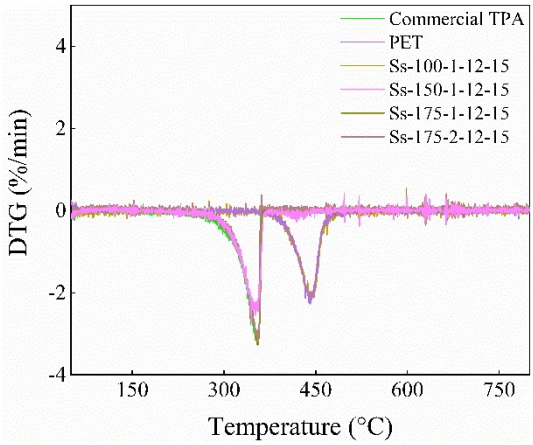

Fig. S9 DTG curves of commercial TPA, PET and S_S-*T*-*m*-*t*-*p* samples.

Before HPLC–MS analysis, the collected solid samples were first dissolved in a small amount of dimethyl sulfoxide (DMSO), then diluted with mobile phase A and filtered through a 0.45 μm needle filter. The HPLC chromatograms of S_S-175-1-12-15 and S_S-175-2-12-15 are shown in Fig. S10.

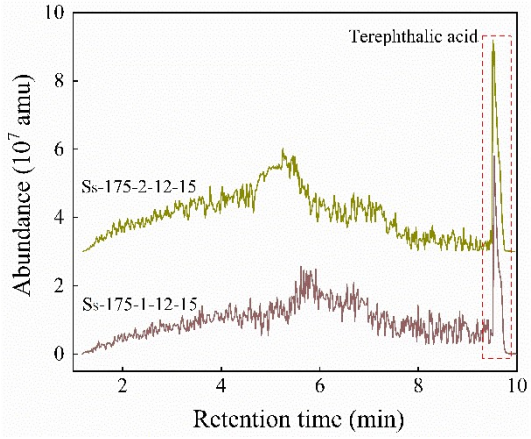

Fig. S10 HPLC signals of S_S-175-1-12-15 and S_S-175-2-12-15 samples. The signals were shifted upward in order by 0 and 3 $\times 10^7$ amu, respectively.

The acidity of $ScCO_2$ and $ScCO_2/H_2O$ was tested using blue litmus paper and universal indicator paper, respectively, and the results are shown in Fig. S11. The blue litmus paper and universal indicator paper exhibited almost no color change in H_2O or $ScCO_2$ alone. However, in the $ScCO_2/H_2O$, the blue litmus paper turned light red and universal indicator paper turned light yellow (pH ≈ 6), which confirmed the acidity of this system.

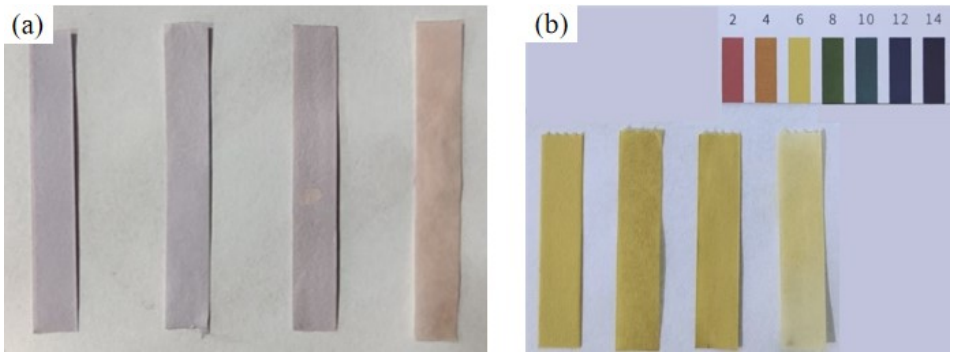

Fig. S11 Color change of (a) blue litmus paper, and (b) universal indicator paper in different system. The reaction environments of paper from left to right were: air, aqueous solution, $ScCO_2$ and $ScCO_2/H_2O$ (the temperature of supercritical fluid is 50°C, the pressure is 15 MPa).

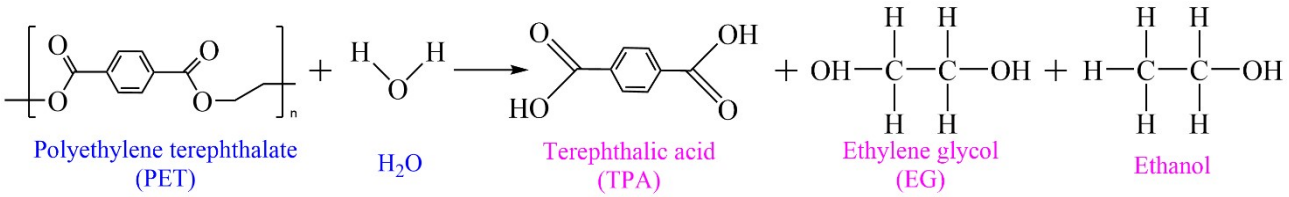

Fig. S12 Hydrolysis process of PET in $ScCO_2$.

Table S3 H_2 evolution activity of PET hydrolysis products in photocatalytic reaction from different reports.

Pretreatment	Photocatalysis	Products	Reference
Reaction in $ScCO_2$ at 175°C for 6 h	300 W Xe lamp, Pt/P25	1416.7 μmol·h^{-1} g^{-1} of H_2 and TPA	This work
Reaction in $ScCO_2$ at 175°C for 12 h	300 W Xe lamp, Pt/P25	1611.2 μmol·h^{-1} g^{-1} of H_2 and TPA	This work
Reaction in 1 M NaOH at 150°C for 24 h	300 W Xe lamp, Pt_{NPs}/TiO_2	219.1 μmol h^{-1} g^{-1} of H_2 and TPA	6
Reaction in 2 M KOH at 60°C for 24 h	100 W Xe lamp with an AM 1.5G filter, Cu/TiO_2 single-atom	193.6 μmol h^{-1} g^{-1} of H_2 and 145.4 μmol h^{-1} g^{-1} of organic acid	7
Reaction in 10 M KOH at 25°C for 48 h	160 W high-pressure UV mercury vapor lamp, Au/TiO_2	451 μmol g_{cat}^{-1} g_{PET}^{-1} of H_2 and 4 mg g_{PET}^{-1} of TPA	8
Ethanol/H_2O 5% NaOH at 25°C for 48 h	160 W high-pressure UV mercury vapor lamp, Au/TiO_2	1925 μmol g_{cat}^{-1} g_{PET}^{-1} of H_2 and 16 mg g_{PET}^{-1} of TPA	8
Reaction in 10 M NaOH at 40°C for 24 h	AM 1.5G, $MoS_2/Cd_xZn_{1-x}S$	15.9 mmol h^{-1} g^{-1} of H_2	9
Reaction in 5 M NaOH at room temperature for 12 h	48 W LED lamp, APS-TFP	77 mmol h^{-1} g^{-1} of H_2 and terephthalate, lactate and glycolate	10
Reaction in 5 M NaOH at 70°C for 72 h	100 W Xe lamp with an AM 1.5G filter, Pt/g−C_3N_4	7.33 mmol h^{-1} g^{-1} of H_2 and TPA	11
Reaction in 5 M KOH at 120°C for 24 h	AM 1.5G, Pt/CPDs−CN	1034 μmol·h^{-1} g^{-1} of H_2 and 304.7 μmol of TPA	12
Reaction in 10 M KOH at 40°C for 48 h	300 W Xe lamp, MoS_2/CdS	3.9 mmol h^{-1} g^{-1} of H_2 and TPA	13
Reaction in 10 M KOH at 70°C for 24 h	500 W Xe lamp, CN−CNTs−NiMo	90 μmol·h^{-1} g^{-1} of H_2	14
Reaction in 10 M KOH	300 W Xe lamp, CdS/NiS	13 mmol h^{-1} g^{-1} of H_2 and	15

at 50°C for 24 h		TPA	
Reaction in 10 M KOH at 60°C for 48 h	500 W mercury lamp, Ni_2P–$Co_2P/ZrO_2/C$	207.56 μmol H_2 g sub^{-1}	16

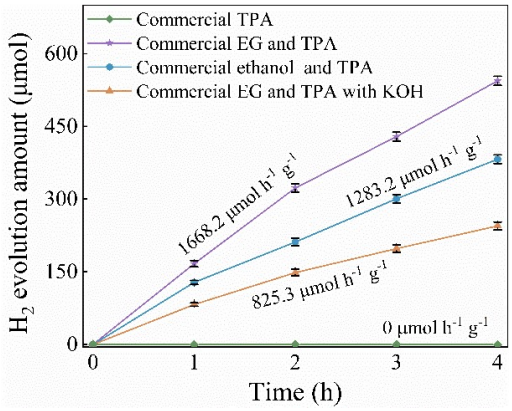

Fig. S13 H_2 evolution curves of commercial TPA, commercial EG and TPA, ethanol and TPA in aqueous solution, and commercial EG and TPA in 1 M KOH solution.

As shown in Fig. 6 and Fig. S14, in the photocatalytic reaction, EG produced from PET hydrolysis was ultimately oxidized into high-value product glycolic acid. The reaction process involved two key stages. Firstly, photogenerated holes initiated α−C−H bond activation in EG. Subsequently, dissolved oxygen was reduced by photogenerated electrons to form reactive oxygen species (ROS, *e.g.*, O_2•$^-$, HO_2•, or H_2O_2), which mediated further oxidation[17, 18]. Upon light irradiation, the photocatalyst generated electron-hole pairs between the valence band and conduction band. The photogenerated holes have strong oxidizing capability, enabling hydrogen abstraction from the α−C−H bond adjacent to the hydroxyl group in EG molecules, thereby achieving preliminary activation of EG. This process caused EG to lose an α-position hydrogen atom, forming the corresponding α-hydroxyalkoxy radical, which further converted into the glycolaldehyde. Simultaneously, photogenerated electrons migrated to the catalyst surface and interacted with dissolved oxygen. As an electron acceptor, oxygen sequentially formed ROS such as O_2•$^-$, HO_2• and H_2O_2 during the reduction process. These highly oxidative ROS continuously oxidized the aldehyde group from the glycolaldehyde into the carboxyl group, ultimately producing glycolic acid.

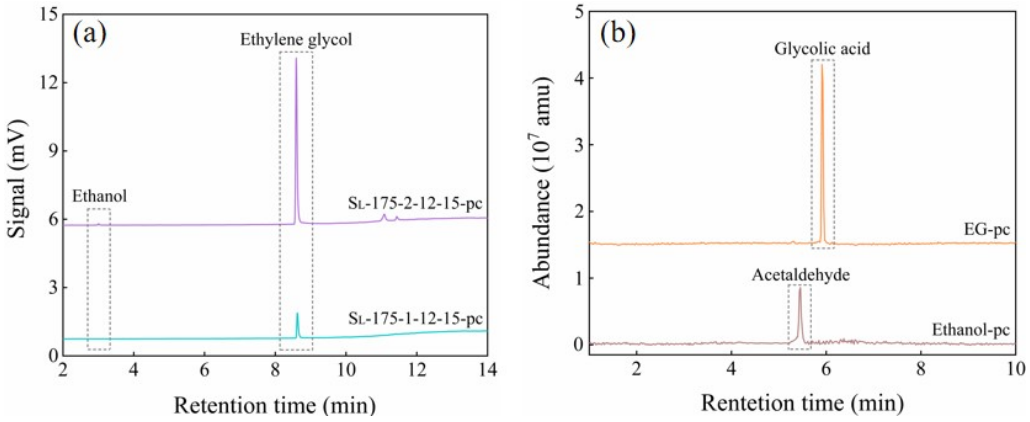

Fig. S14 (a) GC signals of liquid products after photocatalysis, and (b) HPLC signals of liquid products after photocatalysis using commercial EG and ethanol. The signals in (a) were shifted upward in order by 0 and 5 mV, respectively, and (b) were shifted upward in order by 0 and 1.5 ×10^7 amu, respectively.

The solid and liquid products of PET pretreated in $ScCO_2$ were used in photocatalytic reaction, respectively, and the results are shown in Fig. S15. The solid products obtained from PET depolymerization exhibited almost no detectable H_2 during photocatalytic reaction. In contrast, the liquid products of PET depolymerized in $ScCO_2$ played an active role in photocatalytic reaction for H_2 production, which was slightly inferior to the H_2 evolution activity of all products in photocatalytic reaction.

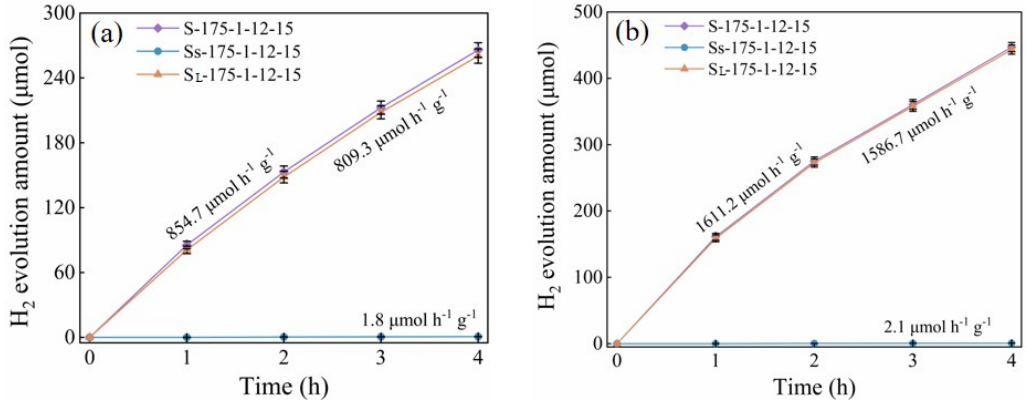

Fig. S15 H_2 evolution curves of different samples in photocatalytic reaction: (a) H_2O/PET mass ratio of 1, and (b) H_2O/PET mass ratio of 2.

References:

1. C. Sun, C. Hou, L. Chen, W. Zhao and Y. Zhang, *Next Energy*, 2025, **8**, 100264.
2. G. Liao, Y. Du, F. Zhang and J. E, *Korean Journal of Chemical Engineering*, 2023, **40**, 11-36.
3. C. Wang, K. R. V. Manikantachari, A. E. Masunov and S. S. Vasu, Determination of the diffusion coefficients of binary CH_4 and C_2H_6 in a supercritical CO_2 environment (500–2000 K and 100–1000 atm) by molecular dynamics simulations, *Energies*, 2024, **17**, 4028.
4. G. Kravanja, M. Škerget, Ž. Knez and M. Knez Hrnčič, *The Journal of Supercritical Fluids*, 2018, **133**, 1-8.
5. C. I. A. V. Santos, M. C. F. Barros and A. C. F. Ribeiro, *Processes*, 2022, **10**, 660.
6. X. Han, M. Jiang, H. Li, R. Li, N. H. M. Sulaiman, T. Zhang, H. Li, L. Zheng, J. Wei, L. He and X. Zhou, *Journal of Colloid and Interface Science*, 2024, **665**, 204-218.
7. Z. Li, Y. Yang, C. Zhang, W. Fan, G. Li, J. Fang and L. Lu, *Chem Catalysis*, 2024, **4**, 100902.
8. E. M. N. Thiloka Edirisooriya, P. S. Senanayake, P. Xu and H. Wang, *Journal of Environmental Chemical Engineering*, 2023, **11**, 111429.
9. Y. Li, S. Wan, C. Lin, Y. Gao, Y. Lu, L. Wang and K. Zhang, *Solar RRL*, 2021, **5**, 2000427.
10. A. Singh, R. Gogoi, K. Sharma, S. K. Jena, N. Fourati, C. Zerrouki, S. Remita and P. F. Siril, *Journal of Cleaner Production*, 2023, **428**, 139476.
11. T. K. A. Nguyen, T. Trần-Phú, X. M. C. Ta, T. N. Truong, J. Leverett, R. Daiyan, R. Amal and A. Tricoli, *Small Methods*, 2024, **8**, 2300427.
12. M. Han, S. Zhu, C. Xia and B. Yang, *Applied Catalysis B: Environmental*, 2022, **316**, 121662.
13. M. Du, Y. Zhang, S. Kang, X. Guo, Y. Ma, M. Xing, Y. Zhu, Y. Chai and B. Qiu, *ACS Catalysis*, 2022, **12**, 12823-12832.
14. X. Gong, F. Tong, F. Ma, Y. Zhang, P. Zhou, Z. Wang, Y. Liu, P. Wang, H. Cheng, Y. Dai, Z. Zheng and B. Huang, *Applied Catalysis B: Environment and Energy*, 2022, **307**, 121143.
15. C. Zhu, J. Wang, J. Lv, Y. Zhu, Q. Huang and C. Sun, *International Journal of Hydrogen Energy*, 2024, **51**, 91-103.
16. W. Qu, X. Qi, G. Peng, M. Wang, L. Song, P. Du and J. Xiong, *Journal of Materials Chemistry C*, 2023, **11**, 14359-14370.
17. L. Roebuck, H. Daly, L. Lan, J. Parker, A. Gostick, N. Skillen, S. J. Haigh, M. Falkowska and C. Hardacre, *Journal of Catalysis*, 2025, **442**, 115876.
18. A. K. Wahab, M. A. Nadeem and H. Idriss, *Frontiers in Chemistry*, 2019, **7**, 780.